Investigation of $\chi^{(2)}$-Translated Optical Frequency Combs Tunability in Gallium Phosphide-on-Insulator Resonators

Pengzhuo Wu, Weiren Cheng, Ning Ding, Xingyu Tang, Zhaoting Geng, Zhenyu Liu, Mingjian You, Xiaolun Yu, Yi Li, and Qiancheng Zhao

***Abstract*—We describe a synergistic optimization approach that enables highly efficient frequency translation of a Kerr optical frequency comb (OFC) from 1550 nm to 775 nm in a gallium phosphide-on-insulator (GaP-OI) microresonator. Key distinctions from previous GaP-OI works which focused on individual optical nonlinearity are that this work not only emphasizes the interaction between the second- and third-order nonlinearity, but also explores the tunability of the $\chi^{(2)}$-translated OFC through geometric and temperature tuning. We apply this approach to the burgeoning GaP-OI platform and demonstrate that a 50 μm-radius ring resonator with a cross-section of 555 nm $\times$ 600 nm has an intracavity second harmonic (SH) generation efficiency as high as 71.5%/W, 3 times larger compared to the state-of-the-art designs. The sum-frequency (SF) comb at 775 nm has a geometric tuning sensitivity of 354 GHz/nm, and a thermal tuning sensitivity of 24.8 GHz/K, paving the way for post-fabrication trimming and in-situ spectral shaping, with a broader potential to realize highly efficient, wide-spectrum, and tunable on-chip nonlinear sources.**

***Index Terms*—Gallium phosphide-on-insulator, Kerr frequency comb, sum frequency generation, integrated nonlinear photonics.**

I. Introduction

NEAR infrared (NIR, λ∼0.75–1.1 μm) frequency combs have garnered tremendous interest in numerous fields, such as optical atomic clocks [1], metrology [2], astronomical spectroscopy [3], biomedical imaging [4], etc. Squeezing optical frequency combs (OFC) into microresonators using optical Kerr effect (OKE) has proven to be an enabling technology, which levitates as broadband coherent light sources with flexible repetition rates, compact sizes, and on-chip integration capability [5]. However, to directly generate bright Kerr frequency combs at the NIR spectrum inside the microresonators remains challenging, partially due to the considerable normal material dispersion and deteriorated optical quality factors at shorter wavelengths. An effective workaround is through cascaded $\chi^{(2)}$ and $\chi^{(3)}$ nonlinear processes [6], [7], in which an NIR frequency comb can be translated from a short wave infrared (SWIR, λ∼1.1–2.5 μm) Kerr frequency comb via $\chi^{(2)}$-based nonlinear processes [8].

The realization of the $\chi^{(2)}$-translated frequency combs needs the interplay of the second- and third-order optical nonlinearity from the waveguiding material. Several platforms, including Si_3N_4 [9], $LiNbO_3$ [10], AlN [11], and 4H-SiC [12], have been explored to generate two-color OFCs based on the cascaded $\chi^{(2)}$ and $\chi^{(3)}$ nonlinear processes. Among them, gallium phosphide (GaP) stands out due to its intriguing nonlinear and linear optical properties [13]. GaP has a conspicuous third-order nonlinearity with $n_2 = 1.9 \times 10^{-17}$ m^{2}W^{-1} [14] and an intrinsic second-order nonlinearity with $d_{36} = 41$ pm/V at 1550 nm [15]. Besides, two-photon absorption can be neglected above 1.1 μm, which renders high power pump in the entire telecommunication bands possible. In addition, GaP has a wide transparent window (0.55–11 μm) covering both the NIR and SWIR spectra. The advantage of its large refractive index ($n > 3$ at C-band) is further enhanced by the gallium phosphide-on-insulator (GaP-OI) architecture [16], [17], [18]. With the help of GaP-OI microresonators, a sum-frequency (SF) frequency comb around 780 nm could be translated from a Kerr frequency comb around 1560 nm through the $\chi^{(2)}$ processes [13]. Despite the observation of the SF OFC in GaP-OI microresonators, a detailed study on the underlying physics of how to regulate the frequency translation process has not yet been performed. It is therefore necessary to dig into the nonlinear dynamics and its tunability of the $\chi^{(2)}$-translated OFCs in GaP-OI resonators.

In this paper, we theoretically explore the tunability of SF OFCs in GaP-OI microresonators. To fulfil the conditions of generating two-color OFCs in a microring resonator, the phase-matching criteria is investigated to simultaneously realize anomalous dispersion for bright Kerr OFC generation as well as high conversion efficiency for sum frequency generation (SFG). For a GaP-OI resonator with a radius of 50 μm, an

Manuscript received 27 December 2023; accepted 8 February 2024. Date of publication 13 February 2024; date of current version 27 February 2024. This work was supported in part by the Basic and Applied Basic Research Foundation of Guangdong Province under Grant 2021B1515120074 and Grant 2023A1515012141, in part by the National Natural Science Foundation of China under Grant 62205137, and in part by the Wuhan National Laboratory for Optoelectronics under Grant 2021WNLOKF001. *(Corresponding authors: Yi Li; Qiancheng Zhao.)*

The authors are with the School of Microelectronics, MOE Engineering Research Center of Integrated Circuits for Next Generation Communications, Southern University of Science and Technology, Shenzhen 518000, China (e-mail: 12232525@mail.sustech.edu.cn; 12231169@mail.sustech.edu.cn; 12333314@mail.sustech.edu.cn; 12333287@mail.sustech.edu.cn; 12010607@mail.sustech.edu.cn; 12333287@mail.sustech.edu.cn; 12333354@mail.sustech.edu.cn; 12111824@mail.sustech.edu.cn; liy37@sustech.edu.cn; zhaoqc@sustech.edu.cn).

This article has supplementary downloadable material available at https://doi.org/10.1109/JPHOT.2024.3365214, provided by the authors.

Digital Object Identifier 10.1109/JPHOT.2024.3365214

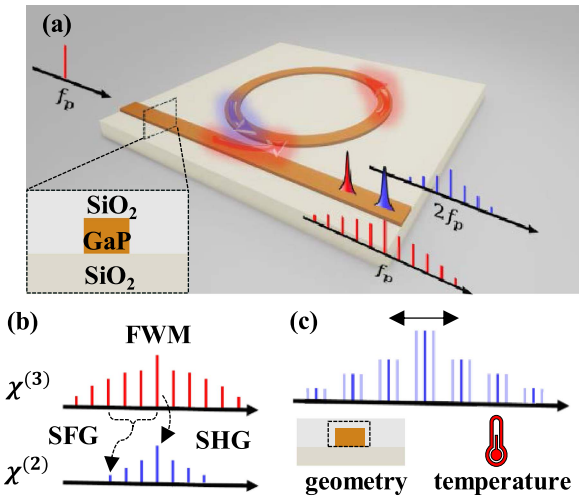

Fig. 1. (a) Schematic of a GaP-OI microresonator that supports OFCs at SWIR and NIR spectra. The inset shows the waveguide cross-section. (b) Mechanism of bright Kerr OFC generation and $\chi^{(2)}$-based OFC frequency translation. (c) Generated SF OFC could be tuned by modifying waveguide geometry or applying temperature change.

optimized waveguide cross-section ($W_{\mathrm{wg}} \times H_{\mathrm{wg}} = 555$ nm $\times$ 600 nm) yields an intracavity second harmonic generation (SHG) conversion efficiency as high as 71.5%/W, 3 times higher than previous work [19]. A Kerr OFC near 1550 nm and an SF comb near 775 nm are simultaneously generated by the coupled Lugiato-Lefever Equation (CLLE). The SF comb spectral profile could be adjusted by modifying the GaP-OI waveguide geometry or altering the temperature. The geometric tuning sensitivity and thermal tuning sensitivity are 354 GHz/nm and 24.8 GHz/K, respectively.

The presented study unleashes the potential to stimulate and manipulate the $\chi^{(2)}$-translated OFCs in GaP-OI microresonators. Thermal tuning is especially useful in selecting the desired up-conversion wavelength, while geometric tuning sheds light on fabrication tolerance as well as post-fabrication analysis. This study is a vital complement to previous experimental work [13], in which modeling and controlling of the $\chi^{(2)}$-based frequency translation were missing. Distinguished from other works of GaP-OI integrated nonlinear devices which solely focused on either second- [17], [18], [20] or third-order [14], [21] nonlinearity, this work emphasizes the frequency translation that links the $\chi^{(3)}$ process and the $\chi^{(2)}$ process, paving the way towards realizing highly efficient two-color frequency combs [15]. What's more, we improved the CLLE model so that it can not only work with the modal phase-matching condition [22] but also the cyclic phase-matching condition which is commonly encountered in ring resonators, extending the application scope of the framework for the nonlinear coupling between the $\chi^{(2)}$ and $\chi^{(3)}$ processes.

II. Device Design and Optimization

An artistic picture of the two-color GaP-OI OFC microresonator is shown in Fig. 1(a). The GaP waveguide sits on the SiO_2 substrate and is embedded in SiO_2 cladding. A continuous

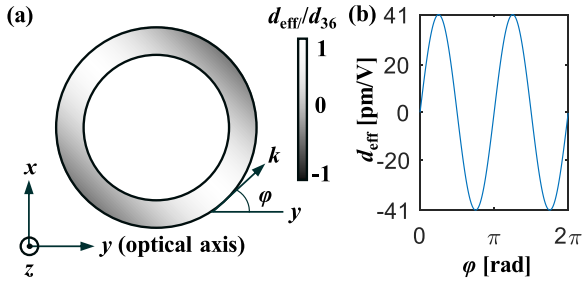

Fig. 2. (a) Schematic of the effective nonlinear susceptibility d_{eff} in a GaP-OI microresonator. (b) d_{eff} versus rotation angle φ.

wave laser with frequency f_{p} is coupled into the resonator to pump bright Kerr OFCs through the four-wave mixing (FWM) process. Meanwhile, frequency translation occurs via the SHG and SFG processes, and SF comb lines around 775 nm emerge as illustrated in Fig. 1(b). During the frequency translation, phase-matching plays an indispensable role since it guarantees momentum conservation of photons to facilitate energy transfer. Geometric modification or temperature tuning can alter the phase-matching point, yielding a tunable SF comb spectral profile as sketched in Fig. 1(c). Another important factor during the frequency translation is the modal overlap which determines the nonlinear conversion efficiency. Based on these two factors, along with the restraint condition of anomalous dispersion for the FWM process, the GaP-OI resonator geometry is investigated accordingly.

A. Phase-Matching for Second-Harmonic Generation and Sum Frequency Generation

Since the non-zero components in the second-order nonlinear susceptibility tensor of GaP are d_{14} (equivalently d_{25} and d_{36}), we choose the low-frequency mode to be TE polarized and the high-frequency mode to be TM polarized, following the Type-I phase-matching criteria. Due to the $\bar{4}3\,\mathrm{m}$ symmetry of (100)-normal GaP crystal, the effective nonlinear susceptibility changes sign every 90° in the wafer plane as shown in Fig. 2, therefore, the cyclic phase-matching condition ought to be used to avoid back conversion [17], [23]. For an axial-symmetric microring structure, the cyclic phase-matching condition of the SFG process manifests itself through the azimuthal mode numbers as follows:

$$\lambda m = n_{\mathrm{eff}} 2\pi R \tag{1}$$

$$|m_3 - (m_1 + m_2)| = 2 \tag{2}$$

where m stands for the azimuthal mode number, λ is the resonant wavelength, n_{eff} is the effective mode index, $R = 50$ μm is the ring radius. Meanwhile, the energy conservation regulates the resonant wavelengths to be,

$$\lambda_3^{-1} = \lambda_1^{-1} + \lambda_2^{-1} \tag{3}$$

where the subscripts 1 and 2 represent the low-frequency modes at the SWIR spectrum, and 3 represents the up-converted mode

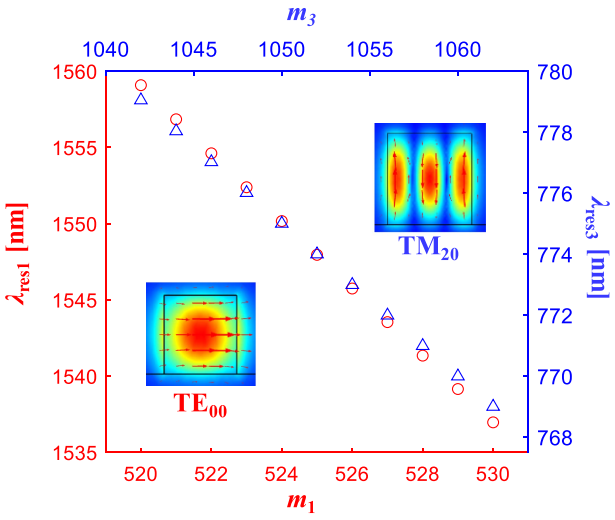

Fig. 3. Phase-matching point of a 555 nm × 600 nm GaP-OI waveguide for the SHG process. The insets show the mode profiles of the low-frequency waveguide mode TE_{00} and high-frequency waveguide mode TM_{20}.

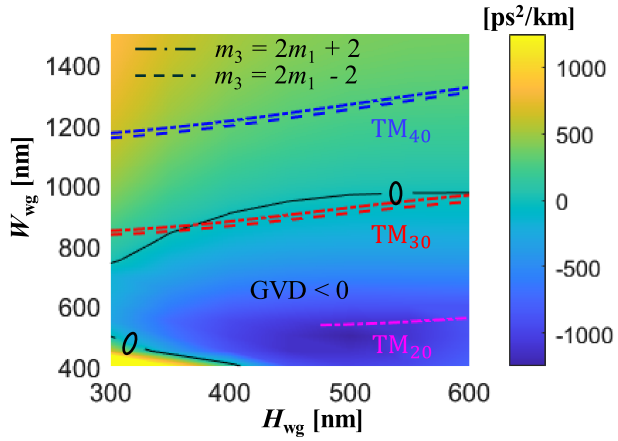

Fig. 4. Colormap of the GVD at 1550 nm under different waveguide geometries. The black contour represents the zero-dispersion location. The chain lines and dashed lines indicate the waveguide geometries that satisfy SHG phase matching conditions of $m_3 = 2m_1 + 2$ and $m_3 = 2m_1 - 2$, respectively, within the 1550 ± 4 nm spectral range.

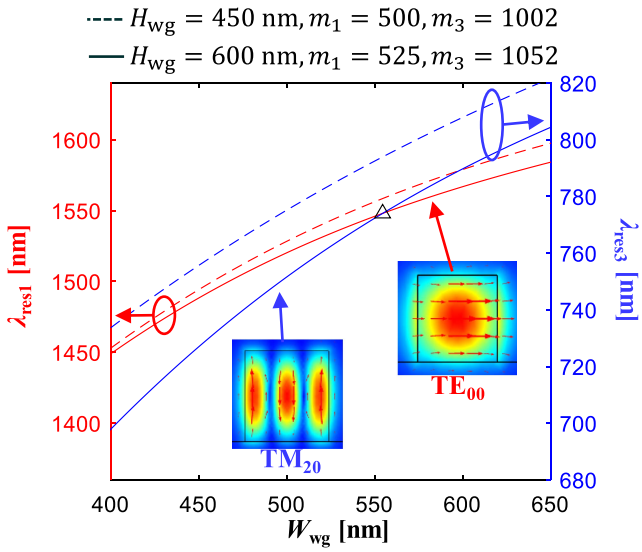

Fig. 5. Resonant wavelength as a function of waveguide width for the TE_{00} and TM_{20} modes in two waveguides with different heights. The triangle represents the phase-matching location. The solid line represents the $H_{wg} = 600$ nm waveguide, and the dashed line represents the $H_{wg} = 450$ nm waveguide.

in the NIR spectrum. For the SHG process, $m_1 = m_2$ and $\lambda_1 = \lambda_2$.

Fig. 3 illustrates the phase-matching point of a 50 μm-radius resonator with a cross-section of 555 nm × 600 nm for the SHG process. The mode number relation demonstrated here is $m_3 = 2m_1 + 2$. As the mode number increases, both the resonant wavelengths for TE_{00} mode and TM_{20} mode decrease following (1), yielding the cross-over at 1548 nm. Thus, the phase-matching mode orders are determined to be $m_1 = 525$ and $m_3 = 1052$. It is worth noting that the phase-matching wavelengths for the pump and SH modes are not exactly at 1550 nm and 775 nm but around them. We believe this is caused by the nature of the discrete resonance. However, such slight wavelength deviations could be compensated conveniently by detuning the pump laser. We assume that ±4 nm wavelength offset is tolerable for practical purposes.

B. Design Space of GaP-OI Waveguides

For bright Kerr OFC generation, anomalous dispersion is required to balance the phase shift induced by the Kerr nonlinearity. Both the material dispersion and waveguide dispersion contribute to the total dispersion, and when it comes to ring resonators, the bending effect should also be considered. We map out the anomalous dispersion region with respect to the waveguide geometry in Fig. 4. The black contour line indicates the location of the zero-dispersion, and the enclosed region represents GVD < 0 at 1550 nm. The colored lines reflect the waveguide geometries that satisfy the cyclic phase-matching condition for the SHG process. Three TM modes can be supported on the map, namely TM_{20}, TM_{30}, and TM_{40}. On one hand, for TM_{30} and TM_{40}, both the $\Delta m = \pm 2$ cases are analyzed for each mode based on (3). On the other hand, the TM_{20} mode fails to meet the requirements of (2) and (3) in the vicinity of 1550 nm for the case of $m_3 - 2m_1 = -2$. Even for the $m_3 - 2m_1 = 2$ case, the TM_{20} mode is cut at the height of 475 nm, below which no phase-matching geometry could be found within the pump wavelength detuning range. To visualize the cutoff effect of TM_{20} mode, the resonant wavelengths for the waveguides with two different heights are compared in Fig. 5. For the waveguide with a height of 600 nm, a phase-matching wavelength around 1550 nm could be found (marked by the triangle), when the waveguide width is 555 nm, and the corresponding m_3 and m_1 are 1052 and 525, respectively. On the contrary, the waveguide with a height of 450 nm fails to find a cross-over wavelength near 1550 nm with m_3 and m_1 derived to be 1002 and 500 from (1).

C. Modal Overlap for Second-Harmonic Generation and Sum Frequency Generation

Besides phase-matching, another factor that determines the second-order nonlinear conversion efficiency is modal overlap.

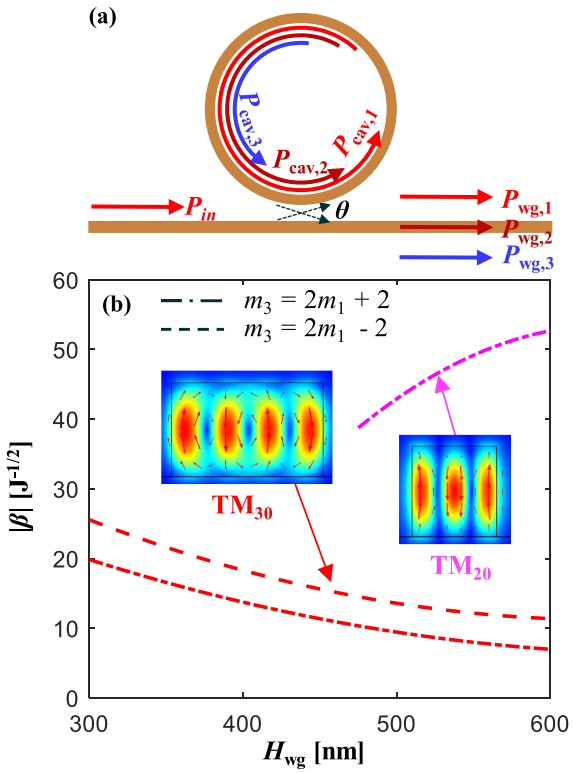

Fig. 6. (a) Illustration of the coupling of the optical power between the bus waveguide and the ring resonator. (b) Nonlinear coupling strength of each geometry and SH modes that satisfy the phase matching condition.

Under pump un-depletion assumption, the small-signal intra-cavity conversion efficiency of the SFG process, η_{cav}, is related to the optical properties of the microresonators as follows [23], [24], [25]

$$\eta_{\text{cav}} = P_{\text{cav},3} / \left(P_{\text{cav},1} P_{\text{cav},2}\right) \tag{4}$$

$$\eta_{\text{cav}} = 8\pi |\beta|^2 \frac{\omega_3^2 R n_{\text{g}1} n_{\text{g}2}}{c n_{\text{g}3} \left(4\Delta^2 + \kappa_3^2\right)} \tag{5}$$

where the subscripts 1 and 2 represent the low-frequency modes in the SWIR spectrum, and 3 represents the up-converted mode in the NIR spectrum. n_{g} is the group index, κ is the total loss rate. $\Delta = \omega_3 - (\omega_1 + \omega_2)$ describes the angular frequency mismatch. P_{cav} is the power in the cavity, and it is related to the power in the output bus waveguide as $P_{\text{wg}} = \theta P_{\text{cav}}$, where θ is the ring-bus power coupling coefficient, as shown in Fig. 6(a). The modal overlap β in the cylindrical coordinate is [24]

$$\beta = \frac{\left|\chi^{(2)}\right|}{4\sqrt{\varepsilon_0}} \frac{\int_{NL} \left[(B_1 - iB_2) e^{i(M+2)\theta} + (B_1 + iB_2)\, e^{i(M-2)\theta}\right] dV}{\sqrt{\int \varepsilon_1 |E_1|^2 dV} \sqrt{\int \varepsilon_2 |E_2|^2 dV} \sqrt{\int \varepsilon_3 |E_3|^2 dV}} \tag{6}$$

where,

$$M = m_1 + m_2 - m_3 \tag{7}$$

$$\begin{aligned} B_1 = {} & E_{1\text{z}}^* \left(E_{2\text{r}}^* \text{conj}(E_{3\theta}) + E_{2\theta}^* \text{conj}(E_{3\text{r}})\right) \\ & + E_{2\text{z}} \left(E_{1\text{r}} E_{3\theta}^* + E_{1\theta} E_{3\text{r}}^*\right) + E_{3\text{z}}^* \left(E_{1\text{r}} E_{2\theta} + E_{1\theta} E_{2\text{r}}\right) \end{aligned} \tag{8}$$

TABLE I
CONVERSION EFFICIENCIES OF SHG INSIDE MICRORESONATORS IN DIFFERENT PLATFORMS

Platform	Reported η_{wg} [%/W]	Estimated η_{cav} [%/W]	Data Type
GaP [17]	425	~1.9	Theoretical
AlN [19]	20000	~28.4	Theoretical
$LiNbO_3$ [28]	1500	~3.6	Experimental
SiC [29]	360	~0.3	Experimental
Si_3N_4 [26]	2500	~5.1	Experimental
GaP (this work)	/	71.5	Theoretical

$$\begin{aligned} B_2 = {} & E_{1\text{z}} \left(E_{2\text{r}} E_{3\text{r}}^* - E_{2\theta} E_{3\theta}^*\right) \\ & + E_{2\text{z}} \left(E_{1\text{r}} E_{3\text{r}}^* - E_{1\theta} E_{3\theta}^*\right) + E_{3\text{z}}^* \left(E_{1\text{r}} E_{2\text{r}} - E_{1\theta} E_{2\theta}\right) \end{aligned} \tag{9}$$

$E_{\text{r}}, E_\theta, E_z$ stand for the three components of the electric field in cylindrical coordinate. They are extracted from a finite-element-method electromagnetic solver. $\chi^{(2)} = 2d_{14}$ is the second-order nonlinear susceptibility which is set to 82 pm/V. The nonlinear modal overlap $|\beta|$ is then used as a figure of merit to optimize the waveguide geometry.

Shown in Fig. 6(b) are the comparisons of the modal overlap for each supported mode in the design space in Fig. 4. TM_{20} outperforms TM_{30} mode, which is attributed to the cancellation of the electric fields with opposite phases in the integral. As the waveguide height increases (correspondingly, the waveguide width also increases as outlined in Fig. 3), the $|\beta|$ of TM_{20} increases because more electric field is confined in the core region. On the contrary, the $|\beta|$ of TM_{30} drops due to a reduction of mode intensity as the waveguide cross-section enlarges. Finally, the waveguide geometry is set to be a $W_{\text{wg}} \times H_{\text{wg}} = 555$ nm $\times$ 600 nm as a comprise of the optimization results and the availability of our GaP epitaxial wafer film stack [14].

The optimized resonator has an intra-cavity SHG conversion efficiency of 71.5%/W, 3 times higher than the state-of-the-art resonator for SH generation [19] to the best of the authors' knowledge. This high conversion efficiency is partially attributed to the optimized mode overlap β. To be specific, the waveguide mode at 775 nm is TM_{20} in our work while that in Ref. [17] is TM_{30} mode. Meanwhile, the GaP material has a larger second-order nonlinear susceptibility ($\chi^{(2)} = 82$ pm/V) than AlN ($\chi^{(2)} = 6.2$ pm/V [19]), Si_3N_4 ($\chi^{(2)} = 0.2$ pm/V [26]), and $LiNbO_3$ ($\chi^{(2)} = 19.5$ pm/V [27]), which also contributes to the high conversion efficiency. It is fair to acknowledge that the conversion efficiency may be lower than its predicted value when measured from real devices. A list of microresonator platforms for SH generation are summarized in Table I. For a fair comparison, the reported waveguide-to-waveguide conversion efficiencies η_{wg} in the previous works are converted to the intracavity conversion

efficiencies η_{cav} using the following equation.

$$\eta_{\text{cav}} = \eta_{\text{wg}} / \left(\mathcal{F}_1^2 \theta_3\right) \tag{10}$$

where $\mathcal{F}$is cavity enhancement of the resonator. Detailed calculations of Table II are included in the supplementary.

III. Frequency Comb Generation

In microresonators with only third-order Kerr nonlinearity, the dynamics of Kerr OFC evolution can be described by the Lugiato-Lefever Equation (LLE) [30], [31]. When there exists second-harmonic nonlinearity inside the cavity, the second-harmonic OFC can be generated simultaneously with the help of nonlinear coupling between the fundamental and second-harmonic waves. We use a set of coupled LLE equations to describe the behavior of the intracavity as follows.

$$t_R \frac{\partial E_1}{\partial t} = \left(-\frac{\alpha_1{}'}{2} + i\delta_0 + iL\sum_{k>1}\frac{\beta_{k,1}}{k!}\left(i\frac{\partial}{\partial\tau}\right)^k + i\gamma_1 L|E_1|^2 + i2\gamma_{13}L|E_3|^2\right)E_1 + i\kappa L E_3 E_1^* + \sqrt{\theta E_{in}} \tag{11}$$

$$t_R \frac{\partial E_3}{\partial t} = \left(-\frac{\alpha_3{}'}{2} + 2i\delta_0 + i\Delta\omega - \Delta k^{'}\frac{\partial}{\partial\tau} + iL\sum_{k>1}\frac{\beta_{k,3}}{k!}\left(i\frac{\partial}{\partial\tau}\right)^k + i\gamma_3 L|E_3|^2 + i2\gamma_{31}L|E_1|^2\right)E_3 + i\kappa^* L E_1^2 \tag{12}$$

where the subscript 1 represents the low-frequency mode at the SWIR spectrum, and 3 represents the second-harmonic mode at the NIR spectrum, E is the complex electric field, t and τ stand for the slow time and fast time, t_{R} is the round trip time, α' is the round trip loss of the field and it includes the ring-bus coupling loss, $\delta_0 = \omega_{\text{p}} - \omega_0$ is the detuning of the pump wavelength away from the resonance wavelength. L is the resonator perimeter, $\Delta k^{'} = k_2' - k_1'$ is the group velocity mismatch, β_k is the dispersion coefficient of the k-th order of each mode, $\gamma = n_2\omega_0/(cA_{\text{eff}})$ is the nonlinear coefficient, c is the speed of light, A_{eff} is the effective mode area, E_{in} is the input electric field. $\kappa = 16\pi\beta n_{\text{eff},1}\sqrt{n_{\text{eff},3}L}/(\sqrt{c}\lambda_1)$ is the nonlinear coupling coefficient proportional to β, n_{eff} is the effective refractive index. Unlike other work that was based on the model phase-matching condition and included $\Delta k = 2k(\omega_{\text{p}})$ - $k(\omega_{2\text{p}})$ to describe the phase mismatch [22], we replace the phase mismatch term with a frequency mismatch term $\Delta\omega = (\omega_3$ - $2\omega_1)$ because the cyclic phase-matching condition naturally comes with a large Δk per the definition of (2). By introducing the frequency mismatching term, the CLLE model is freed from the Δk constraint that only works for the direct phase-matching condition. Instead, the modified CLLE framework does not differentiate the phase-matching conditions, which extends its application scope.

The pump power is coupled into the resonator via a straight bus waveguide. The coupling coefficients as functions of the coupling gap at 1550 nm and 775 nm wavelengths are plotted in Fig. 7, in which the power flow is illustrated in the insets.

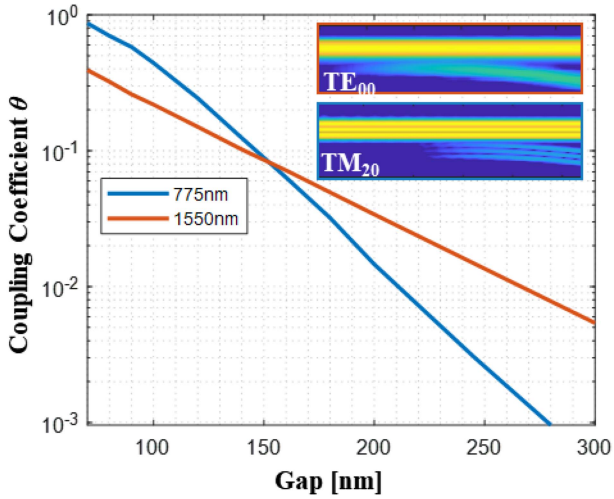

Fig. 7. Coupling coefficient θ versus gap between bus waveguide and resonator of each mode. The inset shows the top view of the coupling of each mode.

The power coupling coefficient of the TE_{00} mode from the bus waveguide to the ring is $\theta = 1.5\%$ when the coupling gap is 245 nm. The waveguide propagation loss is assumed to be 2 dB/cm based on the reported values from the literature [13], [32]. The loaded Q factor at 1550 nm is calculated to be 1.5×10^5. Around 775 nm wavelength, the power coupling coefficient of TM_{20} mode is simulated to be 0.3% from the same coupling region. We assume that the propagation loss increases to 8 dB/cm at shorter wavelengths. Correspondingly, the loaded Q factor at 775 nm is 7.1×10^4.

We first examinate the Kerr OFC spectrum by disabling the nonlinear coupling term in (11) without considering the thermal effect. We repeat the simulation 100 times using the split-step Fourier method (SSFM) to enumerate all possible states of the OFC. With proper selections of pump power and pump detuning, soliton states could be obtained, and their evolution traces are overlaid in Fig. 8(a). The brightness represents the likelihood of each soliton state. The spectra of the 4 soliton states are plotted in Fig. 8(b).

GaP possesses a large thermo-optic coefficient of 1.2×10^{-4} /K [33], which could impede the capture of the solution combs. The impact of the thermal effect on the intracavity field evolution is examinated by introducing an addition phase shift term caused by the thermo-optic effect [34], [35] into (11). Fig. 9 compares the intracavity power versus detuning frequency with (red) and without (blue) the thermo-optic effect of GaP. By properly adjusting the frequency detuning rate, it is possible to acquire a crystal comb state (double soliton pulses in the cavity in this case) theoretically. Detailed calculation of Fig. 9 are included in the supplementary. It is worth noting that soliton states in III-V microresonators have been experimentally demonstrated at room temperature [36]. Thus, to focus on demonstrating the tunability of OFCs, which is the main objective of this paper, we neglect the thermo-optic effect in the following calculations for simplicity purpose.

The NIR OFC can be generated simultaneously along with the fundamental OFC by solving the coupled (11) and (12) together.

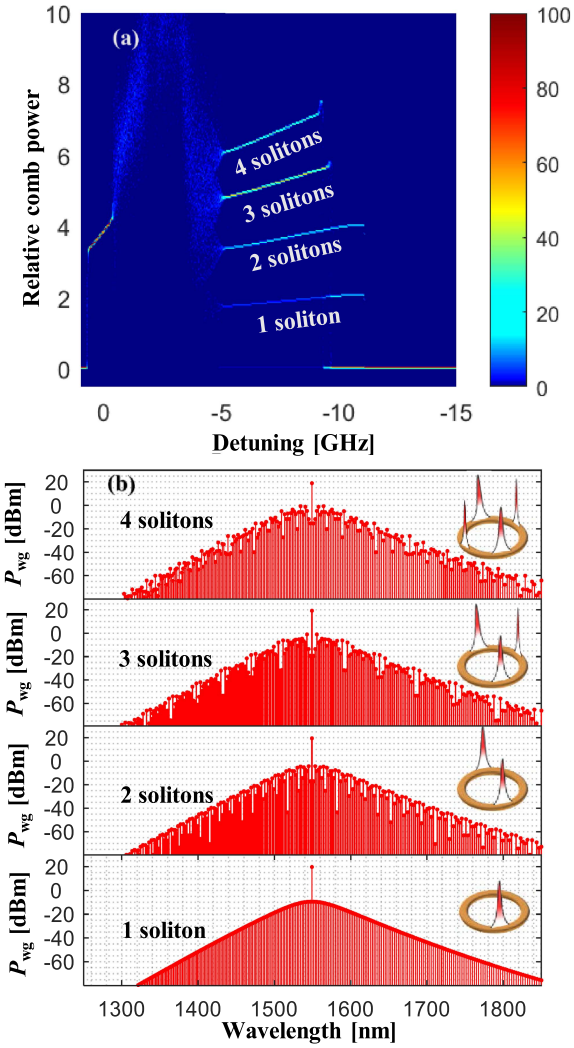

Fig. 8. (a) Relative comb power versus pump detuning of 100 traces are overlaid. The color brightness represents the likelihood of the comb power evolution trace. (b) Spectra of Kerr OFCs from single soliton to four solitons.

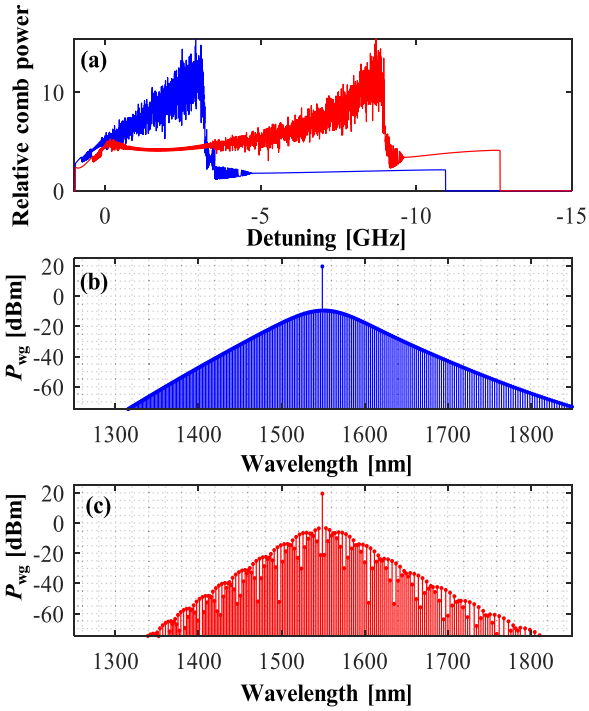

Fig. 9. (a) Relative intracavity comb power versus pump detuning with (red) and without (blue) considering the thermo-optic effect of GaP. (b) The spectrum of a single soliton OFC without the thermo-optic effect. (c) The spectrum of a double soliton OFC with the thermo-optic effect involved.

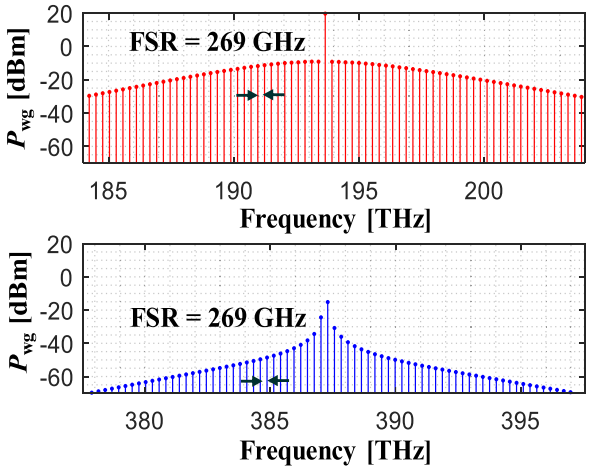

Fig. 10. Generation of an SF OFC (lower) from a Kerr OFC (upper) via $\chi^{(2)}$-based frequency translation. The FSRs of the two combs are the same, proving SFG process is dominant in translation.

As shown in Fig. 10, the free spectral range (FSR) of the NIR OFC is the same as the Kerr OFC as a result of the SFG process. Close to the peak location of the SF OFC, the comb line power is comparable to those in the Kerr OFC, indicating that the existence of the second-harmonic waves cannot be treated as perturbations in this spectral range. As the comb line frequency moves away from the pump frequency, the profile of the fundamental OFC follows a sech^2 profile due to dispersion, while the profile of the SF OFC has a narrower bandwidth due to phase mismatch. Although we focus our attention to the $\chi^{(2)}$-induced frequency translation in this study, it must be noted that the third-harmonic waves resulted from the third-order nonlinearity are also possible in GaP microcavities [23].

IV. Second-Harmonic Frequency Comb Tuning

A. Fabrication Tolerance

Fabrication variation as a commonly encountered hurdle needs to be taken into consideration in the design phase. The lithography and etching steps bring uncertainties to the waveguide dimension, which can deviate the waveguide width from the target value. The influence of waveguide width variation is pictured in Fig. 11(a) where the SF comb power evolves with the varying waveguide width from 550 nm to 560 nm. There are two bright yellow lines. The narrow and dim one represents the SH tone that is frequency-doubled from the pump wavelength, and the thicker and brighter one reflects the SF comb peak. As shown in Fig. 11(b), the SF comb spectral peak does not necessarily align with the SH tone, because the SH tone wavelength is determined by the pump wavelength, while the SF comb peak wavelength, where the maximum SFG conversion

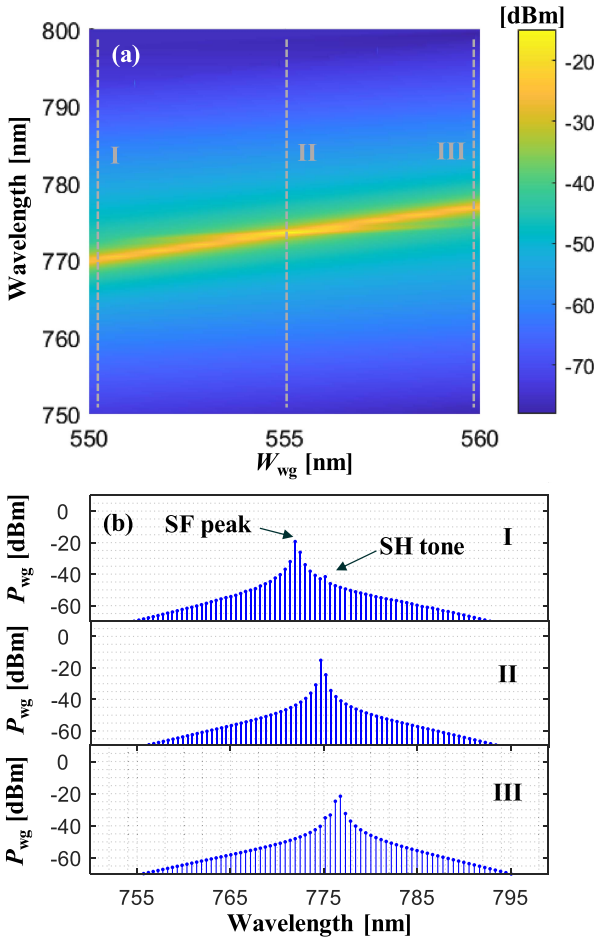

Fig. 11. Geometric tuning analysis of microring resonator. (a) Relationship between waveguide width and power envelope of SF comb. (b) Envelope of SF OFC with varying waveguide width and fixed $H_{wg} = 600$ nm.

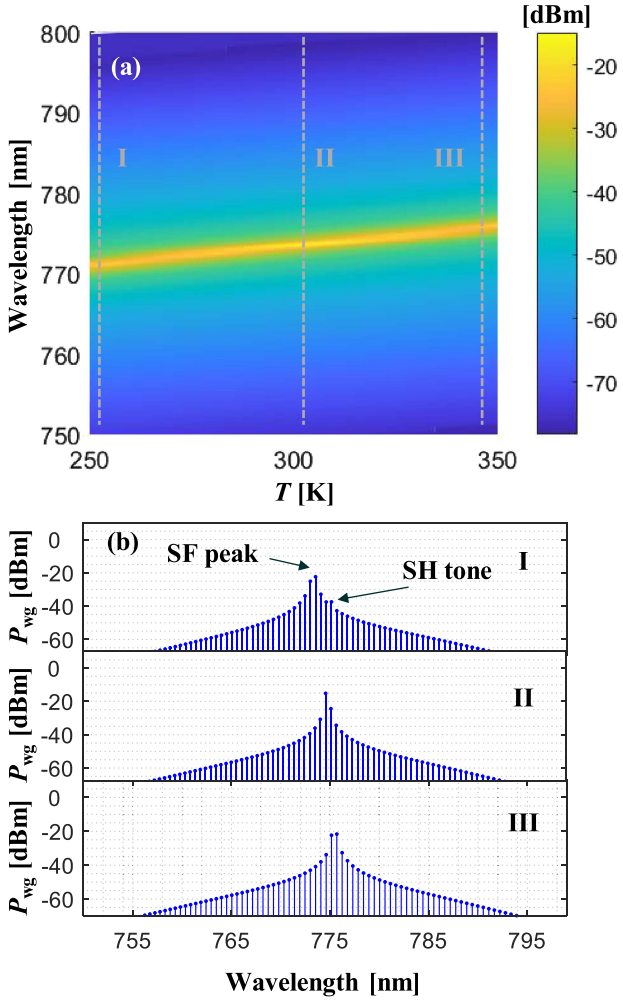

Fig. 12. Thermal regulation analysis of microring resonator. (a) Relationship between temperature and power envelope of SF comb. (b) Envelope of SF OFC with varying temperature and fixed $H_{wg} = 600$ nm and $W_{wg} = 555$ nm.

happens, is regulated by the cyclic phase-matching condition. As the waveguide width increases, the phase-matching wavelengths both around 1550 nm and around 775 nm have red-shift. The movement of the former one is less than the latter. The SF comb peak shifts from the $m_3 = 1058$ to the $m_3 = 1049$ mode order within ± 5 nm width variation, corresponding to a tuning sensitivity of 354 GHz/nm, while the pump wavelength has a tuning sensitivity of 110 GHz/nm. The geometric sensitivity of the pump wavelength is directly translated to the SH tone, leading to a less sensitive frequency drift rate of the SH tone compared to the SF comb peak. As the waveguide width variation further increases, the separation between the SH tone and SF comb peak wavelength becomes more pronounced. Besides phase-matching locations, the conversion efficiency is also subject to change due to the waveguide width variation. The power of the SF comb peak drops 8.9 dB when the waveguide width varies 5 nm due to the mismatch between $\chi^{(2)}$ phase matching point and the discrete comb lines on the wavelength scale.

B. Temperature Tuning

The dependence of the SF comb spectrum on the waveguide geometry is two sides of the same coin. On one hand, it opens the possibility to post-trim the fabricated devices to approach the desired spectrum [18], [37]. On the other hand, it lays stringent requirements on the fabrication tolerance. Fortunately, the fabrication constraints can be relaxed by thermal tuning. The GaP material has a thermo-optic coefficient of 1.2×10^{-4} K^{-1} near 1550 nm and 1.6×10^{-4} K^{-1} near 775 nm [33]. The SF comb profiles with respect to the device temperature are depicted in Fig. 12(a). As the temperature changes, the phase-matching wavelength also varies, red-shifting the envelope of the SF comb and reducing the conversion efficiency. The SF comb profiles at three different temperatures are compared in Fig. 12(b). Within 100 K temperature variation, the SF comb peak shifts from the mode order $m_3 = 1055$ to $m_3 = 1051$, corresponding to a tuning sensitivity of 24.8 GHz/K. Thus, thermal tuning is verified to fine tune the comb spectra.

V. Conclusion

In summary, we demonstrate that manipulation on the SF OFC spectrum could be realized in GaP-OI microresonators via geometric or temperature tuning. The waveguide dispersion

and phase-matching condition are synergistically optimized in order to fulfill the bright Kerr OFC and SFG prerequisites. The optimized ring resonator has a cross-section of $W_{wg} \times H_{wg} = 555$ nm $\times$ 600 nm with a radius of 50 μm, which enables a prominent intracavity SFG conversion efficiency as high as 71.5%/W. Kerr OFC and SF OFC are numerically solved using the CLLE. Both the SF comb spectrum and the conversion efficiency can be controlled by the waveguide geometry and temperature, leaving a geometric and thermal sensitivity of 354 GHz/nm and 24.8 GHz/K, respectively. The presented study theoretically opens the possibility of controlling the $\chi^{(2)}$-translated optical frequency combs, paving the way towards a deeper understanding of the nonlinear coupling between the $\chi^{(2)}$ and $\chi^{(3)}$ nonlinear processes [22], [38]. The two-color OFC GaP-OI microresonator in principle suggests a new paradigm for highly efficient and tunable nonlinear optical sources which could find wide applications in frequency metrology, quantum photonics, and biophotonics.

REFERENCES

[1] Z. L. Newman et al., "Architecture for the photonic integration of an optical atomic clock," *Optica*, vol. 6, no. 5, pp. 680–685, May 2019, doi: 10.1364/OPTICA.6.000680.

[2] S.-P. Yu et al., "Tuning kerr-soliton frequency combs to atomic resonances," *Phys. Rev. Appl.*, vol. 11, no. 4, Apr. 2019, Art. no. 044017, doi: 10.1103/PhysRevApplied.11.044017.

[3] M. T. Murphy et al., "High-precision wavelength calibration of astronomical spectrographs with laser frequency combs," *Monthly Notices Roy. Astronomical Soc.*, vol. 380, no. 2, pp. 839–847, Sep. 2007, doi: 10.1111/j.1365-2966.2007.12147.x.

[4] P. J. Marchand et al., "Soliton microcomb based spectral domain optical coherence tomography," *Nature Commun.*, vol. 12, no. 1, Jan. 2021, Art. no. 427, doi: 10.1038/s41467-020-20404-9.

[5] A. L. Gaeta, M. Lipson, and T. J. Kippenberg, "Photonic-chip-based frequency combs," *Nature Photon.*, vol. 13, no. 3, pp. 158–169, Mar. 2019, doi: 10.1038/s41566-019-0358-x.

[6] A. W. Bruch et al., "Pockels soliton microcomb," *Nature Photon.*, vol. 15, no. 1, pp. 21–27, Jan. 2021, doi: 10.1038/s41566-020-00704-8.

[7] D. N. Puzyrev and D. V. Skryabin, "Carrier-resolved real-field theory of multi-octave frequency combs," *Optica*, vol. 10, no. 6, Jun. 2023, Art. no. 770, doi: 10.1364/OPTICA.487008.

[8] L. Chang, S. Liu, and J. E. Bowers, "Integrated optical frequency comb technologies," *Nature Photon.*, vol. 16, no. 2, pp. 95–108, Feb. 2022, doi: 10.1038/s41566-021-00945-1.

[9] S. Miller, K. Luke, Y. Okawachi, J. Cardenas, A. L. Gaeta, and M. Lipson, "On-chip frequency comb generation at visible wavelengths via simultaneous second- and third-order optical nonlinearities," *Opt. Exp.*, vol. 22, no. 22, pp. 26517–26525, Nov. 2014, doi: 10.1364/OE.22.026517.

[10] Y. He et al., "Self-starting bi-chromatic $LiNbO_3$ soliton microcomb," *Optica*, vol. 6, no. 9, pp. 1138–1144, Sep. 2019, doi: 10.1364/OPTICA.6.001138.

[11] X. Guo et al., "Efficient generation of a near-visible frequency comb via cherenkov-like radiation from a kerr microcomb," *Phys. Rev. Appl.*, vol. 10, no. 1, Jul. 2018, Art. no. 014012, doi: 10.1103/PhysRevApplied.10.014012.

[12] C. Wang et al., "Soliton formation and spectral translation into visible on CMOS-compatible 4H-silicon-carbide-on-insulator platform_supplementary," *Light Sci. Appl.*, vol. 11, no. 1, Dec. 2022, Art. no. 341, doi: 10.1038/s41377-022-01042-w.

[13] D. J. Wilson et al., "Integrated gallium phosphide nonlinear photonics," *Nature Photon.*, vol. 14, no. 1, pp. 57–62, Jan. 2020, doi: 10.1038/s41566-019-0537-9.

[14] W. Cheng et al., "Wafer-scale inverted gallium phosphide-on-insulator rib waveguides for nonlinear photonics," *Opt. Lett.*, vol. 48, no. 14, pp. 3781–3784, Jul. 2023, doi: 10.1364/OL.494949.

[15] H. Ji et al., "High-power two-color Kerr frequency comb generation on the gallium phosphide-on-insulator platform at SWIR and MIR spectra," *J. Opt. Soc. Amer. B Opt. Phy.*, vol. 40, no. 8, pp. 1976–1985, Aug. 2023, doi: 10.1364/JOSAB.492194.

[16] K. Schneider, P. Welter, Y. Baumgartner, H. Hahn, L. Czornomaz, and P. Seidler, "Gallium phosphide-on-silicon dioxide photonic devices," *J. Lightw. Technol.*, vol. 36, no. 14, pp. 2994–3002, Jul. 2018.

[17] A. D. Logan et al., "400%/W second harmonic conversion efficiency in 14 μm-diameter gallium phosphide-on-oxide resonators," *Opt. Exp.*, vol. 26, no. 26, pp. 33687–33699, Dec. 2018, doi: 10.1364/OE.26.033687.

[18] L. Thiel et al., "Precise electron beam-based target-wavelength trimming for frequency conversion in integrated photonic resonators," *Opt. Exp.*, vol. 30, no. 5, pp. 6921–6933, Feb. 2022, doi: 10.1364/OE.446244.

[19] A. W. Bruch et al., "17 000%/W second-harmonic conversion efficiency in single-crystalline aluminum nitride microresonators," *Appl. Phys. Lett.*, vol. 113, no. 13, Sep. 2018, Art. no. 131102, doi: 10.1063/1.5042506.

[20] A. P. Anthur et al., "Second harmonic generation in gallium phosphide nano-waveguides," *Opt. Exp.*, vol. 29, no. 7, pp. 10307–10320, Mar. 2021, doi: 10.1364/OE.409758.

[21] Z. Geng et al., "Dispersion-flattened concentric structure for microcomb bandwidth broadening in GaP-OI resonators," *J. Opt. Soc. Amer. B Opt. Phy.*, vol. 40, no. 3, pp. 673–681, Mar. 2023, doi: 10.1364/JOSAB.477493.

[22] X. Xue et al., "Second-harmonic-assisted four-wave mixing in chip-based microresonator frequency comb generation," *Light Sci. Appl.*, vol. 6, no. 4, Apr. 2017, Art. no. e16253, doi: 10.1038/lsa.2016.253.

[23] B. McLaughlin, D. P. Lake, M. Mitchell, and P. E. Barclay, "Nonlinear optics in gallium phosphide cavities: Simultaneous second and third harmonic generation," *J. Opt. Soc. Amer. B*, vol. 39, no. 7, Jul. 2022, Art. no. 1853, doi: 10.1364/JOSAB.455234.

[24] A. D. Logan et al., "Triply-resonant sum frequency conversion with gallium phosphide ring resonators," *Opt. Exp.*, vol. 31, no. 2, pp. 1516–1531, Jan. 2023, doi: 10.1364/OE.473211.

[25] X. Liu et al., "Generation of multiple near-visible comb lines in an AlN microring via $\chi^{(2)}$ and $\chi^{(3)}$ optical nonlinearities," *Appl. Phys. Lett.*, vol. 113, no. 17, Oct. 2018, Art. no. 171106, doi: 10.1063/1.5046324.

[26] X. Lu, G. Moille, A. Rao, D. Westly, and K. Srinivasan, "Efficient photoinduced second harmonic generation in silicon photonics," *Nature Photon.*, vol. 15, no. 2, pp. 131–136, Feb. 2021, doi: 10.1038/s41566-020-00708-4.

[27] J. Lu et al., "Periodically poled thin-film lithium niobate microring resonators with a second-harmonic generation efficiency of 250,000%/W," *Optica*, vol. 6, no. 12, pp. 1455–1460, Dec. 2019, doi: 10.1364/OPTICA.6.001455.

[28] R. Luo, Y. He, H. Liang, M. Li, J. Ling, and Q. Lin, "Optical parametric generation in a lithium niobate microring with modal phase matching," *Phys. Rev. Appl.*, vol. 11, no. 3, Mar. 2019, Art. no. 034026, doi: 10.1103/PhysRevApplied.11.034026.

[29] D. M. Lukin et al., "4H-silicon-carbide-on-insulator for integrated quantum and nonlinear photonics," *Nature Photon.*, vol. 14, no. 5, pp. 330–334, May 2020, doi: 10.1038/s41566-019-0556-6.

[30] G. T. Moille, Q. Li, X. Lu, and K. Srinivasan, "pyLLE: A fast and user friendly lugiato-lefever equation solver," May 2019, Accessed: Nov. 13, 2021. [Online]. Available: https://www.nist.gov/publications/pylle-fast-and-user-friendly-lugiato-lefever-equation-solver

[31] L. A. Lugiato, F. Prati, M. L. Gorodetsky, and T. J. Kippenberg, "From the Lugiato–Lefever equation to microresonator-based soliton Kerr frequency combs," *Philos. Trans. Roy. Soc. A: Math., Phys. Eng. Sci.*, vol. 376, no. 2135, Dec. 2018, Art. no. 20180113, doi: 10.1098/rsta.2018.0113.

[32] A. Nardi et al., "Soliton microcomb generation in a III-V photonic crystal cavity," Apr. 2023. Accessed: Aug. 07, 2023. [Online]. Available: https://arxiv.org/abs/2304.12968v2

[33] J. Wei, J. M. Murray, J. O. Barnes, P. G. Schunemann, and S. Guha, "Temperature dependent Sellmeier equation for the refractive index of GaP," *Opt. Mater. Exp.*, vol. 8, no. 2, pp. 485–490, 2018.

[34] S. Wang et al., "Pump condition dependent Kerr frequency comb generation in mid-infrared," *Results Phys.*, vol. 15, Dec. 2019, Art. no. 102789, doi: 10.1016/j.rinp.2019.102789.

[35] T. Carmon, L. Yang, and K. J. Vahala, "Dynamical thermal behavior and thermal selfstability of microcavities," *Opt. Exp.*, vol. 12, no. 20, pp. 4742–4750, 2004.

[36] L. Wu et al., "AlGaAs soliton microcombs at room temperature," *Opt. Lett.*, vol. 48, pp. 3853–3856, May 2023, doi: 10.1364/OL.484552.

[37] G. Moille, D. Westly, N. G. Orji, and K. Srinivasan, "Tailoring broadband Kerr soliton microcombs via post-fabrication tuning of the geometric dispersion," *Appl. Phys. Lett.*, vol. 119, no. 12, Sep. 2021, Art. no. 121103, doi: 10.1063/5.0061238.

[38] X. Guo, C.-L. Zou, L. Jiang, and H. X. Tang, "All-optical control of linear and nonlinear energy transfer via the zeno effect," *Phys. Rev. Lett.*, vol. 120, no. 20, May 2018, Art. no. 203902, doi: 10.1103/PhysRevLett.120.203902.